Interface Engineering of Needle-Like P-Doped MoS_2/CoP Arrays as Highly Active and Durable Bifunctional Electrocatalyst for Overall Water Splitting

Yan Hu,[a] Hongbo Yu,[a] Luoluo Qi,[a] Jiaxin Dong,*[a] Puxuan Yan,[a] Tayirjan Taylor Isimjan,*[b] and Xiulin Yang*[a]

Developing a bifunctional water splitting catalyst with high efficiency and low cost are crucial in the electrolysis water industry. Here, we report a rational design and simple preparation method of MoS_2-based bifunctional electrocatalyst on carbon cloth (CC). The optimized P-doped MoS_2@CoP/CC catalyst presents low overpotentials for the hydrogen (HER) and oxygen evolution reactions (OER) of 64 and 282 mV in alkaline solution as well as 72 mV HER overpotential in H_2SO_4 at a current density of 10 mA cm^{-2}. Furthermore, P-MoS_2@CoP/CC as a bifunctional catalyst delivered relatively low cell voltages of 1.83 and 1.97 V at high current densities of 500 and mA cm^{-2} in 30% KOH. The two-electrode system showed a remarkable stability for 30 h, even outperformed the benchmark RuO_2||Pt/C catalyst. The excellent electrochemical performance can be credited to the unique microstructure, high surface area, and the synergy between metal species. This study presents a possible alternative for noble metal-based catalysts to overcome the challenges of industrial applications.

Introduction

At present, the energy depletion issue has aroused widespread concern and become an obstacle to economic development.[1] Developing a sustainable hydrogen economy has become a hot topic in the scientific world.[2] Electrocatalytic overall water splitting is considered as a sustainable approach of large-scale hydrogen generation hydrogen production from water. The two half reactions in the water splitting are hydrogen evolution reaction (HER) and oxygen evolution reaction (OER).[3] The commercial water splitting systems are currently run at 1.8–2.4 V cell voltage and 200–400 mA cm^{-2} current density.[4] Therefore, anything higher than 200 mA cm^{-2} is considered high current density. Since the OER half-reaction is the rate-determining step, most of the electrolyzers are operated under alkaline conditions, where the HER kinetics is two orders of magnitude slower than in acidic conditions. Therefore, it is critical to develop low-overpotential HER catalysts in alkaline media. In addition, it is especially interesting if the HER catalyst also shows an excellent OER performance because the bifunctional catalyst will primarily simplify the production process and decrease the cost. To date, metal-based catalysts such as Pt-based materials and Ru oxides are still recognized as the most effective HER and OER catalysts, respectively.[5] However, their high cost and the inadequate resources of precious metals limit their extensive commercial applications. As a result, considerable attention has been devoted to developing earth-abundant transition metal-based HER and OER catalysts with performance comparable to these precious metal catalysts.[6]

Recently, transition metal-based electrocatalysts and their derivatives, including metal chalcogenides,[7] metal phosphides,[4a,8] and metal carbides[9] were reported as HER/OER bifunctional electrocatalysts. Still, they suffered from slow kinetics and low stability.[10] Among them, Mo-based catalysts revealed great potential. Density function theory (DFT) studies revealed that MoS_2 could exhibit excellent HER performance in acidic media due to the edge sites resulting in optimal hydrogen adsorption free energies ($\triangle G \approx 0.08$ eV).[11] However, the HER performance worsens in alkaline solutions because of surface-adsorbed hydroxyl species that hinder the water dissociation steps.[12] To address this problem, Hu et al.[13] proposed a combination of MoS_2 with layered double hydroxides (LDHs) materials, including Ni, Co, and Fe that are well-known OER catalysts. As a result, the HER kinetics of MoS_2-LDH catalysts were accelerated significantly due to the improved binding and dissociation kinetics of hydroxyl species. Besides, a MoO_2–Ni/carbon cloth (CC) heterostructure exhibited high hydrogen evolution performance over the entire pH range.[14] Similarly, an MoS_2@CoS_2 electrocatalyst with rich structural defects has also shown high hydrogen evolution performance and outstanding durability.[15] The HER performance of Mo-based catalysts can be further improved by phosphorus doping.[16] Moreover, heterostructured MoS_2/NiS_2 revealed excellent HER and OER performance in alkaline electrolytes because of the synergy between Ni and Mo species and OER nature of the Ni-based catalysts.[17] Many studies have shown

[a] Y. Hu, H. Yu, L. Qi, J. Dong, P. Yan, Prof. Dr. X. Yang
Guangxi Key Laboratory of Low Carbon Energy Materials
School of Chemistry and Pharmaceutical Sciences
Guangxi Normal University
Guilin 541004 (P. R. China)
E-mail: chemdjx@gxnu.edu.cn
xlyang@gxnu.edu.cn
[b] Dr. T. Taylor Isimjan
Saudi Arabia Basic Industries Corporation (SABIC) at King Abdullah University of Science and Technology (KAUST)
Thuwal 23955-6900 (Saudi Arabia)
E-mail: isimjant@sabic.com

Supporting information for this article is available on the WWW under https://doi.org/10.1002/cssc.202002873

that as a promising OER catalyst,[18] introducing cobalt-based phosphide into HER catalyst can improve its performance.[19] As a result, MoS_2 is coupled with cobalt-based phosphides and phosphorous doping to enhance HER performance in alkaline media further. It was envisioned that Mo-based materials facilitate HER/OER kinetics in alkaline media by facilitating binding and dissociation kinetics of the hydroxyl species. As compared to the commonly available methods in the literature,[20] including high-temperature annealing of metal-organic framework (MOF) precursors, we used a moderate temperature in situ thermal growth followed by drip-coating and PH_3 chemical vapor deposition approach that results in needle-like nanoarrays on the CC support. The prepared P-MoS_2@CoP/CC materials can be directly used as a self-supported electrode, which is easier to scale up than the traditional powder system.

Here, we developed a facile and controllable method to construct P-doped MoS_2@CoP/CC heterostructure catalyst. Three steps of the catalyst preparation are: 1) growing Co(OH)F nanowire arrays on CC, 2) quantitatively pipetting ammonium thiomolybdate (3 wt% of $(NH_4)_2MoS_4$ in DMF), and 3) phosphorization treatment. The microstructure, crystallinity, and chemical state of the resulting P-MoS_2@CoP/CC were characterized and analyzed in detail. Electrochemical studies showed that the optimized catalyst show low overpotentials of 64 mV (HER, Figure S1 in the Supporting Information) and 282 mV (OER) at 10 mA cm^{-2} in 1.0 M aqueous KOH. Furthermore, the catalyst exhibits two-electrode cell voltages of 1.83 and 1.97 V at 500 and 1000 mA cm^{-2} as well as long-term stability for overall water splitting in 30% alkaline solution, implying a potential commercial application.

Results and Discussion

Synthesis strategy and structural analysis

The synthetic processes of the P-MoS_2@CoP/CC are illustrated in Figure 1, and photographs of different samples are shown in Figure S2. The hydrothermal deposition procedure was used to prepare Co(OH)F array in situ grown on CC, and the corresponding crystal structure was confirmed as orthorhombic Co(OH)F (JCPDS: 50-0827) by X-ray diffraction (XRD; Figure S3). Then, ammonium thiomolybdate (3 wt% of $(NH_4)_2MoS_4$ in DMF) was used to prepare the support's surface with different loadings. Finally, a series of hybrid precursors are phosphated to P-doped MoS_2@CoP/CC via PH_3 gas produced by NaH_2PO_2 pyrolysis. The inductively coupled plasma (ICP) results (Table S1) indicate that the maximum MoS_2 loading was around 70 wt%. TEM elemental mappings revealed that MoS_2 was well dispersed on the surface of the CoP nanowire arrays. XRD crystal phase analysis shows that the diffraction peaks of the obtained P-MoS_2@CoP/CC can be well indexed to the standard diffraction patterns of CoP (JCPDS: 29-0497) and MoS_2 (JCPDS: 37-1492),[19c,21] respectively (Figure 2a). The strong diffraction peak at ~25° belongs to the (002) lattice plane of graphitic carbon.[22] Notably, the XRD patterns of CoP/CC and P-MoS_2/CC are very similar to these of P-MoS_2@CoP/CC (Figure S4).

The surface morphologies of the materials were characterized by scanning electron microscopy (SEM). Figure S5a shows a smooth CC surface before the in situ growth of Co(OH)F species. A thin layer of a needle-like nanoarray structure was formed (Figure S5b) after Co(OH)F deposition. Furthermore, the CoP/CC morphology remained the same during the phosphorizing treatment (Figure S5c). After P-doped MoS_2 decoration, a thin layer of P-doped MoS_2 was formed on the CoP nanoneedles surface (Figure 2b, c). As the concentration of the Mo precursor increases, the surface coverage of the CoP nanoneedles becomes denser (Figure S5d, e). Notably, the surface of P-MoS_2-modified CC shows severe aggregation without a Co(OH)F buffer layer (Figure S5f).

Transmission electron microscopy (TEM) was used to further study the microstructure features of the P-MoS_2@CoP/CC. Figure 2d shows that the thickness of the P-MoS_2 species modified on the surface of the CoP nanoarray is about 95 nm. The high-resolution (HR)-TEM image shows two types of lattice fringes (Figure 2e) that correspond to the lattice spacing of 0.162 nm (301) and 0.245 nm (102) of the orthorhombic CoP crystal planes. The other set corresponds to the (105) and (106) crystal planes of hexagonal MoS_2 with lattice spacings of 0.183 and 0.164 nm.[23] The formed heterostructure was also confirmed by selected area electron diffraction (SAED; Figure 2f). The TEM images show the diffraction spots of (200) and (211) corresponding to CoP and (106) for MoS_2.[19c,24] Moreover, the high-angle annular dark field (HAADF) TEM elemental mappings suggest that Co, Mo, P, and S are distributed uniformly in P-MoS_2@CoP/CC (Figure 2g).

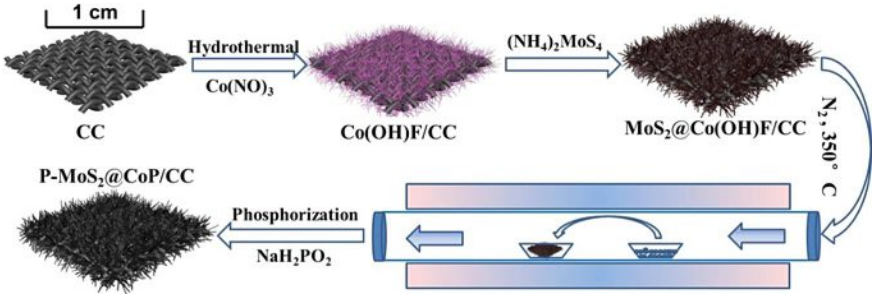

Figure 1. Schematic illustration of the synthesis of P-MoS_2@CoP/CC.

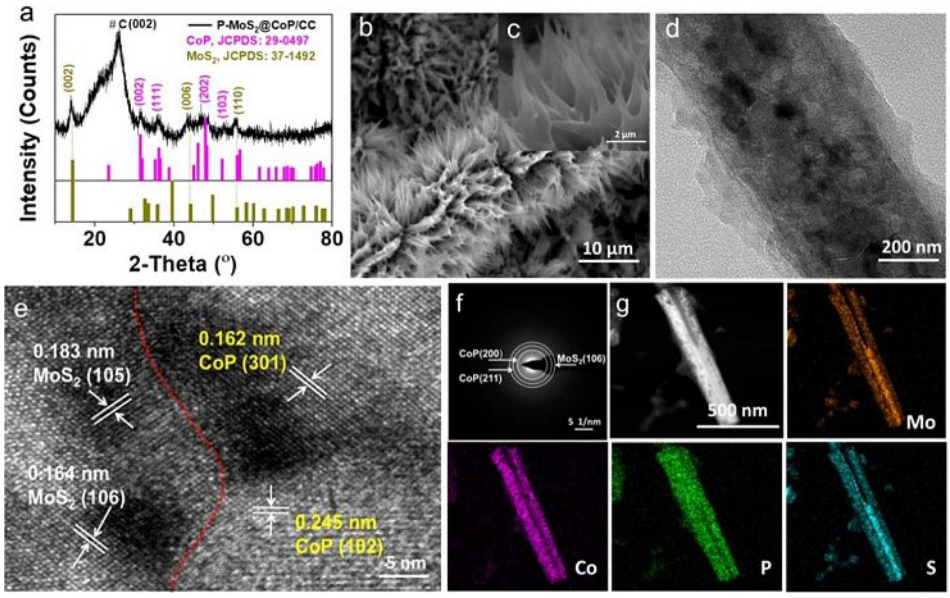

Figure 2. a) XRD patterns of P-MoS_2@CoP/CC. b, c) SEM images of P-MoS_2@CoP/CC. d) TEM image, e) HR-TEM image and f) SAED of P-MoS_2@CoP/CC. g) HAADF-TEM image and corresponding elemental mappings of P-MoS_2@CoP/CC (color online).

The nitrogen adsorption-desorption isotherms of CoP and P-MoS_2@CoP (scraped off the CC) show a typical type Ш behavior (Figure S6). The isotherm data indicate that the Brunauer-Emmett-Teller (BET) surface area of CoP and P-MoS_2@CoP are 15 and 13 $m^2 g^{-1}$, accompanying Barrett-Joyner-Halenda (BJH) average pore size distributions are 30 and 12 nm, respectively. This change could be due to the reduced surface area resulting from P-MoS_2 modification, which shortens the gaps between the needle-like structures.[20b] The high porosity of P-MoS_2@CoP is beneficial for mass transfer and access to more active sites. Moreover, the experimental results indicate an apparent synergistic effect between the two species. The two distinctive features of P-MoS_2@CoP jointly improve electrochemical performance.[25]

XPS analysis

The chemical composition and surface electronic states of P-MoS_2@CoP/CC were investigated by X-ray photoelectron spectroscopy (XPS). XPS survey spectra illustrate that the P-MoS_2@CoP/CC's surface is mainly composed of Co, Mo, P, S, O, C, and N elements (Figure S7a). The C 1s spectrum of P-MoS_2@CoP/CC can be deconvoluted into C=C (284.0 eV), C–C (284.8 eV), and C–O (286.0 eV) used as calibration standard (Figure S7b).[26] As for Mo 3d in Figure 3a, it can be deconvoluted into four subpeaks. The peaks at 226.4, 229.1, and 230.5 eV are assigned to S 2 s, 2H-Mo-S, and 1T-Mo-S, respectively.[27] Compared to P-MoS_2/CC, the binding energy of 1T-Mo-S of P-MoS_2@CoP/CC is slightly shifted to higher binding energies (about 0.48 eV). In Figure 3b, Co 2p can be fitted to synthesize six subpeaks and divided into three pairs of CoP (779.4 eV), Co–O (781.8 eV) and one satellite peak (785.5 eV).[19c,28] Inversely, the binding energy of Co–P of P-MoS_2@CoP/CC exhibit a negative shift of 0.5 eV relative to CoP/CC. The S $2p_{1/2}$ and S $2p_{3/2}$ peaks of P-MoS_2@CoP/CC are located at 163.1 and 161.9 eV, respectively, which corresponds to MoS_2 (Figure 3c).[29] Similarly, as shown in Figure 3d, the P 2p XPS of P-MoS_2@CoP/CC with the peaks of P $2p_{1/2}$ and P $2p_{3/2}$ located at 130.7 and 129.8 eV are ascribed to P–Mo and/or P–Co.[19c,30] The clear shifts in binding energy illustrate that the charge redistribution occurs between the two spices due to the strong interaction between Co and Mo species at the interface of P-MoS_2@CoP.[7b,31] The charge transfer from Mo to Co species on the interface increases the electrical conductivity of the material,[32] thereby helping to improve HER and OER performance.

Electrocatalytic HER analysis

The HER performance of the heterogeneous P-MoS_2@CoP/CC catalyst was measured in 1.0 M KOH using a standard three-electrode system. The P-MoS_2@CoP-2 catalyst only needs 64 and 141 mV to reach the current densities of 10 and 100 mA cm^{-2} in 1.0 M KOH (Figure 4a, b). These results are comparable with Pt/C (overpotentials: $\eta_{10}=48$ mV, $\eta_{100}=125$ mV), and much smaller than those of other control catalysts (Table S2), such as MoS_2@Co(OH)F ($\eta_{10}=179$ mV, $\eta_{100}=267$ mV), CoP ($\eta_{10}=140$ mV, $\eta_{100}=222$ mV), MoS_2 ($\eta_{10}=102$ mV, $\eta_{100}=$ mV), P-MoS_2@CoP-1 ($\eta_{10}=80$ mV, $\eta_{100}=161$ mV) and P-MoS_2@CoP-3 ($\eta_{10}=80$ mV, $\eta_{100}=170$ mV). More importantly, the overpotential of P-MoS_2@CoP-2 is close to that of Pt/C at a current density of 100 mA cm^{-2}, indicating that this interface-engineered electrode can achieve a similar HER performance as a Pt-based catalyst in alkaline media. Notably, the linear sweep

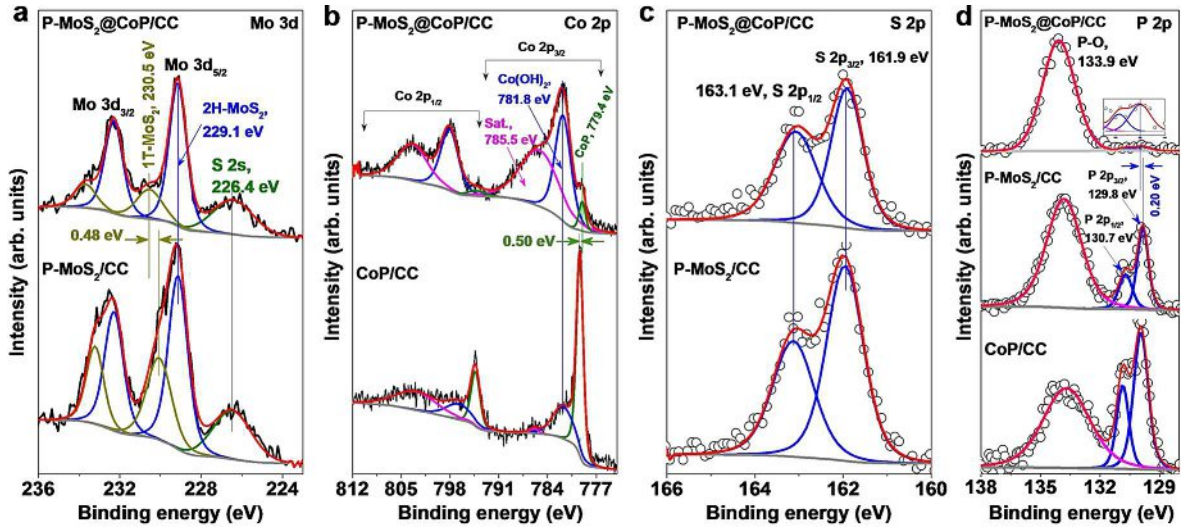

Figure 3. High-resolution XPS spectra of the a) Mo 3d and b) Co 2p and c) S 2p and d) P 2p regions of P-MoS_2@CoP/CC, P-MoS_2/CC, and CoP/CC, respectively.

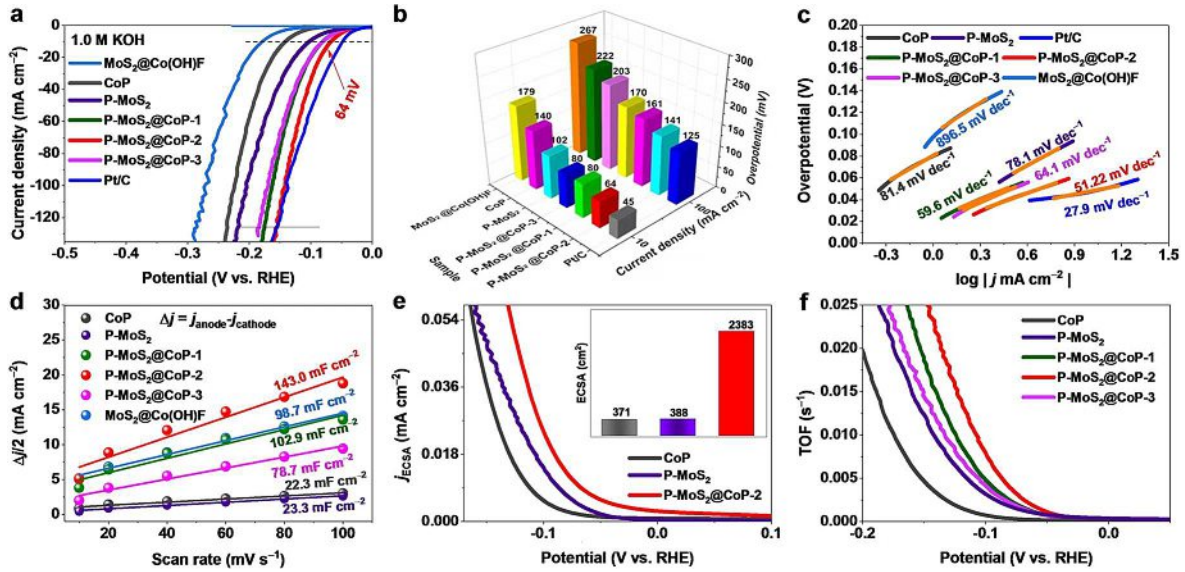

Figure 4. Electrocatalytic HER performance: a) LSV polarization curves, b) comparison of overpotentials at 10 and 100 mA cm^{-2} for P-MoS_2@CoP-2 and other references, c) corresponding Tafel slopes, d) C_{dl} of different catalysts in 1.0 M KOH. (e) ECSA-normalized LSV curves (Inset: a bar chart of the ECSA) of CoP, P-MoS_2, and P-MoS_2@CoP-2. f) Potential-dependent TOF curves of CoP, P-MoS_2, P-MoS_2@CoP-1, P-MoS_2@CoP-2, and P-MoS_2@CoP-3, respectively.

voltammetry (LSV) polarization curve fluctuation at higher current densities is caused by bubbles forming on the electrode surface. The gas bubbles minimize the contact surface area between the electrode and the electrolyte. The current increases again after the gas bubbles leave the surface. Tafel plots were calculated from the polarization curves and are used to investigate the HER kinetic mechanism and the rate-determining steps. In Figure 4c, the Tafel slope of P-MoS_2@CoP-2 (51.2 mV dec^{-1}) is smaller than other samples, indicating that the Volmer–Heyrovsky reaction pathway ($H_2O + e^- \rightleftarrows H_{ads} + OH^-$ and $H_{ads} + H_2O + e^- \rightleftarrows H_2 + OH^-$) is the rate-determining step in alkaline media.[14] The exchange current density, as shown in Figure S8a, is obtained by extrapolating the Tafel slope. The exchange current density of P-MoS_2@CoP-2 is 0.50 mA cm^{-2} was higher than most of the control catalysts, indicating faster electrode dynamics.[14] In addition, electrochemical impedance spectra (EIS) in Figure S8b showed that P-MoS_2@CoP-2 has the lowest charge-transfer resistance (R_{ct}), suggesting an effective electron transfer between catalyst and electrolyte improving HER performance.[25b,33] The smallest R_{ct} could result from the higher conductivity of P-doped MoS_2 and the strong electronic interactions between the P-MoS_2 and CoP species.[34]

The double layer capacitance (C_{dl}) is obtained from a non-faradaic potential region in cyclic voltammetry (CV) graphs of the catalyst at different scan rates (Figure S9). Figure 4d shows that P-MoS_2@CoP-2 has the largest C_{dl} proportional to the

electrochemically surface area (ECSA), providing more HER-active sites.[35] As expected, the P-MoS_2@CoP-2 catalyst retains the maximum ECSA of 2383 cm^2 (normalized to per cm^2 of electrode area), which is much higher than that of CoP (371 cm^2) and P-MoS_2 (388 cm^2) (inset: Figure 4e). The values of C_{dl} and ECSA are close to those of some recently reported Co/Mo-based electrocatalysts (Table S3). A similar trend is also shown in the HER catalytic activity in ECSA-normalized LSV curves (Figure 4e).[35] The optimized catalyst has the highest surface area that exposes more active sites, therefore has a higher ECSA. To evaluate the intrinsic activity of HER, the turnover frequency (TOF) was used to compare the kinetics of the catalysts. The TOF value was calculated using the ICP results. As shown in Figure 4f, the TOF value of P-MoS_2@CoP-2 increased more rapidly compared to P-MoS_2@CoP-1, P-MoS_2@CoP-3, P-MoS_2, and CoP when the applied potential was increased, suggesting that the introduction of an appropriate amount of Mo species improves the intrinsic activity of the Co–Mo dual active site, thereby enhancing HER catalytic activity. Furthermore, P-MoS_2@CoP-2 can maintain long-term stability under a constant current density of -100 mA cm^{-2} with almost no degradation in HER catalytic performance (Figure S10). Besides, a CV test was also used to explore the catalyst's stability. The results reveal that the polarization curve remained almost the same after 3000 cycles (Figure S11). However, there are slight changes in catalyst morphology (Figure S12).

Additionally, the needle-like array electrode also revealed excellent HER performance in acidic media. Similar to the HER activities in 1.0 M KOH, the performance of the catalyst in acidic media follows the order Pt/C > P-MoS_2@CoP > CoP > P-MoS_2 (Figure S13a). The overpotential of P-MoS_2@CoP/CC is only 72 mV at 10 mA cm^{-2}, higher than that of commercial Pt/C (η_{10} = 30 mV) but lower than that of other transition-metal catalysts (Table S4). Figure S13b shows that the Tafel slope of P-MoS_2@CoP/CC is 59.7 mV dec^{-1}, indicating that the Volmer-Heyrovsky reaction pathway is the rate-determining step in acidic solutions.[19c] Moreover, P-MoS_2@CoP/CC shows a smaller R_{ct}, indicating that there is a faster electron transfer for HER (Figure S13c). C_{dl} was calculated from CV curves in the non-faradaic region (Figure S14a–d). Figure S14e shows that the P-MoS_2@CoP/CC catalyst has the largest C_{dl}, demonstrating that the P-MoS_2@CoP/CC catalyst has more effective active sites at the interface between P-MoS_2 and CoP in P-MoS_2@CoP/CC, which synergistically enhances the intrinsic HER activity in acidic media.[36] Additionally, the study found that the catalyst could be continuously operated at -100 mA cm^{-2} for 80 h in 0.5 M H_2SO_4 with almost no degradation (Figure S15). The SEM images (Figure S16) before and after the durability test reveal some changes in the morphology of the catalyst. However, the changes do not affect the catalytic performance, meaning the initial morphology is not a critical factor.

We also studied the HER performance in a neutral electrolyte (pH = 7). The LSV polarization curves showed that the overpotentials of P-MoS_2@CoP/CC, as well as the control catalysts at -10 mA cm^{-2}, were in the range of 138–221 mV. Notably, the overpotential increases rapidly with the increase of current density (Figure S17), which is still far lower than those in alkaline and acid electrolytes.

Electrocatalytic OER analysis

Another critical reaction of total water splitting is OER, so the catalyst's OER performance has been further explored in an alkaline solution. P-MoS_2@CoP/CC requires a low overpotential of 278 mV to reach 10 mA cm^{-2} (Figure 5a). When the current density is 70 mA cm^{-2}, the catalytic performance of P-

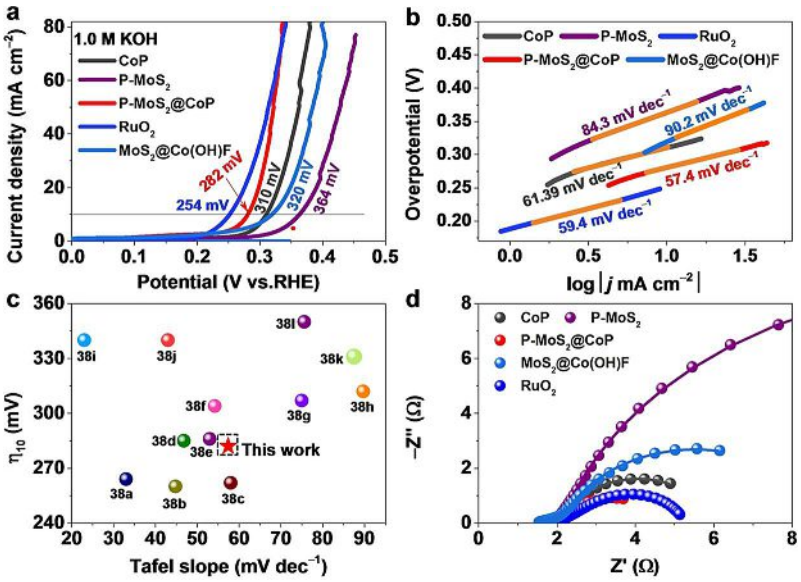

Figure 5. Electrocatalytic OER performance in 1.0 M KOH. a) LSV polarization curves and b) corresponding Tafel slopes of different catalysts. c) Overpotentials of recently reported catalysts at 10 mA cm^{-2}; corresponding Tafel slopes are reported in Table S5. d) Nyquist plots of different catalyst.

MoS_2@CoP/CC exceeds that of RuO_2. Figure 5b displays the corresponding Tafel plots, and the Tafel slope value of P-MoS_2@CoP/CC is 57.4 mV dec^{-1}, revealing favorable 4e$^-$ oxidation kinetics for conversion of water to O_2 on the P-MoS_2@CoP/CC catalyst.[37] Notably, the P-MoS_2@CoP/CC catalyst has a favorable performance comparable to those of recently reported non-precious metal-based electrocatalysts (Figure 5c, Table S5).[38] The lower R_{ct} of P-MoS_2@CoP/CC is attributed to the formation of the heterostructure with metallic composite, leading to improved charge transfer at the P-MoS_2@CoP interface, which eventually accelerates OER reaction (Figure 5d).[39] These results demonstrate that, to some extent, the interfacial interactions of P-MoS_2@CoP/CC between P-MoS_2 and CoP can accelerate the electron transfer and improve the OER catalytic performance. However, the OER stability of the P-MoS_2@CoP/CC catalyst over a long period showed a slight decrease in catalytic activity at a constant current density of 100 mA cm^{-2} for 80 h (Figure S18), which could be due to the partial oxidation of Mo and Co species under robust oxidative environment. There is no noticeable change before and after the durability test (Figure S19).

Overall water splitting analysis

The two-electrode water splitting study is a crucial standard to evaluate whether catalysts can be commercialized.[25b] We first tested the HER and OER performance of the optimized catalyst at high current density (Figure S20). We found that the catalyst only requires HER and OER overpotentials of 458 and 570 mV to reach 1000 mA cm^{-2}, respectively. Subsequently, we used the optimum P-MoS_2@CoP/CC as bifunctional electrocatalyst for overall water splitting in 1.0 M KOH (Figure 6a). The overall water splitting voltages of the bifunctional P-MoS_2@CoP$^{(+/-)}$ catalyst are 1.68, 1.94, and 2.10 V to achieve current densities of 100, 500, and 1000 mA cm^{-2}, respectively (Figure 6b). Notably, the cell voltage of the bifunctional P-MoS_2@CoP$^{(+/-)}$ is slightly lower than the state-of-the art $RuO_2^{(+)}$||Pt/C$^{(-)}$ when the current density exceeds 1000 mA cm^{-2}. Besides, the optimized electrolyzer had a lower cell voltage at 100 mA cm^{-2} compared to most recently reported two-electrode catalytic systems (Figure 6c, Table S6).[2a,40] Figure 6d shows that the bifunctional P-MoS_2@CoP$^{(+/-)}$ catalyst could be continuously operated at 500 mA cm^{-2} for 40 h. We can notice a slight decline after about 37 h, which may be related to structural destruction (Figure S21) and surface chemical state changes (Figure S22) of the hybrid material. Notably, the surface content ratio of 1T-MoS_2 in P-MoS_2@CoP decreased, and CoP almost disappeared after the stability test (Figure S22), indicating that the surface's chemical states had changed during the catalytic process due to the excessive oxidation (OER) and reduction (HER) environments.

The excellent water splitting performance can be discussed as follows. Partial substitution of S by the lower electronegative P will address the low conductivity and high overpotentials of pristine MoS_2. In addition, P doping causes a drop of ΔG_{H^*} (H* is adsorbed intermediate) of the neighboring S atoms in the basal plane to 0.43 eV compared to that of pristine MoS_2 (2.2 eV).[16a] Therefore, H* desorption becomes more accessible, thereby improving HER performance. In addition, different loadings of P-MoS_2 on the surface of the CoP arrays result in significantly different HER performance and R_{ct} values, indicating that the interface between CoP and P-MoS_2 plays an important role in HER catalysis. The water dissociation is the rate-determining step of HER in alkaline media. A DFT study reveals that

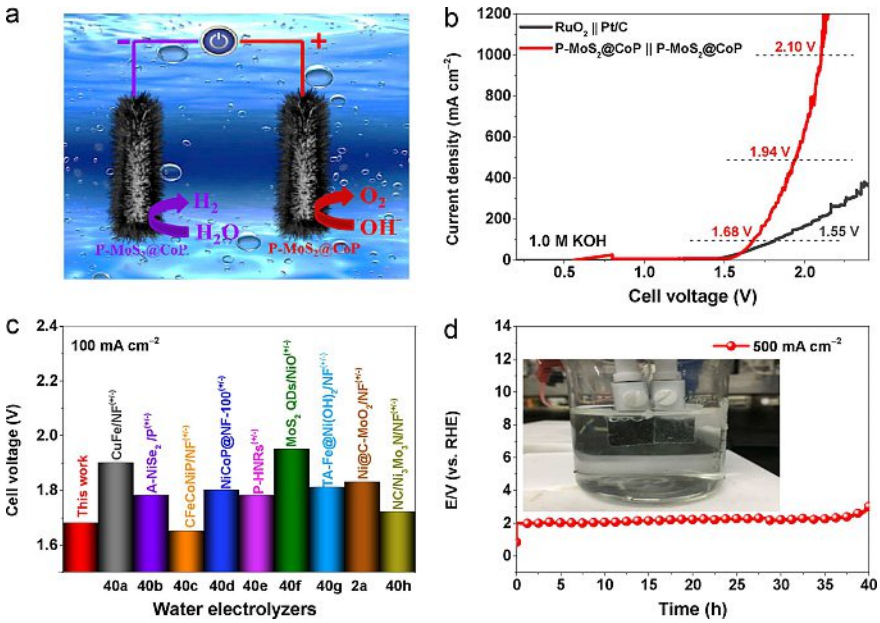

Figure 6. a) Schematic description of overall water splitting in a two-electrode system. b) Polarization curves of the bifunctional P-MoS_2@CoP$^{(+/-)}$ and $RuO_2^{(+)}$||Pt/C$^{(-)}$ catalysts for overall water splitting. c) Comparison of the cell voltages between the optimal P-MoS_2@CoP$^{(+/-)}$ and other electrocatalysts reported in literature. d) Chronopotentiometry curve of the bifunctional P-MoS_2@CoP$^{(+/-)}$ at a current density of 500 mA cm^{-2} in 1.0 M KOH.

unoccupied 3d and 4d transition metal sites in CoP not only act as oxophilic sites to activate water molecule but also modulate the electronic structure of CoP to accelerate the kinetics.[41] The charge transfer between Mo and Co spaces revealed by XPS in P-MoS_2@CoP hybrid structure indicates such synergy that improves the water dissociation, thereby causing faster kinetics. Moreover, the OER performance also is enhanced for P-doped MoS_2 due to the improved P intercalation in MoS_2 resulting in better electron transport.[42] During OER, the surface of CoP is partially oxidized to Co oxides/oxyhydroxides (CoO_x).[43] The in situ-formed CoO_x and P-MoS_2 interfaces can significantly reduce chemisorption free energy for oxygen-containing intermediates.[31] These results indicate that the interfaces constructed between CoP and P-MoS_2 as well as CoO_x and P-MoS_2 are critical for water splitting, which are responsible for enhancing electrochemical hydrogen and oxygen evolutions, respectively.[31,43b]

Conclusions

We have successfully constructed a highly active P-MoS_2@CoP bifunctional catalyst through a facile and controllable method. The P-MoS_2@CoP/carbon cloth (CC) catalyst's heterostructured interface can enrich the active sites, promote electron transfer, and regulate the binding energy of intermediates. All those functions are beneficial for electrocatalytic reactions. Further, the nanoarray structure in situ grown on the conductive CC can provide an effective way for charge transport and open channels for the rapid release of gas bubbles during OER or HER. Various electrochemical test results confirmed a positive P-doping effect. The optimized catalyst revealed HER performance comparable with Pt/C in both acidic and alkaline solutions at high current densities. Moreover, the optimized P-MoS_2@CoP/CC catalyst outperformed RuO_2 on OER. Notably, the cell voltage of P-MoS_2@$CoP^{(+)}$||P-MoS_2@$CoP^{(-)}$ is slightly lower than the state-of-the-art $RuO_2^{(+)}$||$Pt/C^{(-)}$ at a current density of 1000 mA cm^{-2}. This work provides a new strategy to rationally design and construct efficient interface engineering catalysts for overall water splitting.

Experimental Section

Materials

Cobalt nitrate hexahydrate ($Co(NO_3)_2 \cdot 6H_2O$, 99.0%), ammonium tetrathiomolybdate ($(NH_4)_2MoS_4$, 99.95%), urea (CH_4N_2O, $\geq$99.0%), ammonium fluoride (NH_4F, $\geq$96.0%), and sodium hypophosphite monohydrate (NaH_2PO_2, 99.0%) were analytical reagents and used without further purification. Commercial Pt/C (20 wt% Pt) was purchased from Alfa Aesar. RuO_2 powder was synthesized by directly calcining $RuCl_3$ in air at 400 °C.

Synthesis of Co(OH)F nanowires arrays on CC (Co(OH)F/CC)

To a 70 mL deionized water were added 4 mmol $Co(NO_3)_2 \cdot 6H_2O$, 4 mmol NH_4F, and 10 mmol CH_4N_2O. The solution was vigorously stirred for 0.5 h and labeled solution (A). A piece of CC (1 cm × 4 cm) was cleaned ultrasonically in 0.5 M H_2SO_4, water, and ethanol for 15 min to remove impurities, respectively. Then the CC was placed in a Teflon-lined stainless-steel autoclave along with 100 mL of solution (A). The autoclave was sealed and maintained at 120 °C for 10 h and then cooled down slowly at room temperature. The resulting pink CC was taken out and rinsed with deionized water and dried under vacuum at 60 °C. The obtained sample was named Co(OH)F/CC, and the theoretical loading was 2.0 mg cm^{-2}.

Synthesis of P-MoS_2@CoP Nanoarray on CC

To synthesize P-doped MoS_2@CoP, the obtained Co(OH)F/CC was drop-coated with an ammonium thiomolybdate solution (3 wt% of $(NH_4)_2MoS_4$ in DMF), followed by drying under vacuum for 8 h. Then, MoS_2@Co(OH)F/CC and NaH_2PO_2 were put apart in a porcelain boat with 1.0 g NaH_2PO_2 on the upstream side of the tube furnace. Subsequently, the samples were heated to 350 °C at 5 °C min^{-1} and kept for 2 h at this temperature under a N_2 atmosphere, and then naturally cooled to ambient temperature. In this hybrid catalyst, the $(NH_4)_2MoS_4$ loadings were about 3.6, 4.8, and 6.0 mg cm^{-2}, and the resulting samples are marked as P-MoS_2@CoP/CC-1, −2, and −3, respectively. Note that if not specifically stated, P-MoS_2@CoP/CC refers to P-MoS_2@CoP/CC-2. As a control, CoP nanoarray-modified CC (CoP/CC) was prepared using a similar method as mentioned above without $(NH_4)_2MoS_4$. In addition, P-MoS_2/CC was synthesized by directly casting ammonium thiomolybdate solution onto CC (4.8 mg cm^{-2}), followed by a similar phosphorizing treatment.

Characterization

Morphologies and microstructures of the designed materials were characterized by scanning electron microscopy (SEM, Quanta FEG 200, Holland) and transmission electron microscopy (TEM, JEOL, JEM-2100F). X-ray powder diffraction (XRD) data was performe by a D/Max 2500 V PC with $Cu_{K\alpha}$ radiation. The chemical states of the catalyst were analyzed by X-ray photoelectron spectroscopy (XPS, model: JPS-9010 TR Photoelectron Spectrometer, Japan). The catalyst loadings were determined by inductively coupled plasma atomic emission spectrometry (ICP-AES, IRIS Intrepid II XSP). The specific surface area and pore size distribution were calculated according to the BET and BJH methods, respectively.

Electrochemical measurements

The electrocatalytic activity tests were performed on an Biologic VMP3 electrochemical work station with a standard three-electrode system in alkaline and acidic solutions. The catalysts, graphite plate, and standard calomel electrode (SCE) were used as working, counter, and reference electrodes, respectively. A cyclic voltammetry (CV) test to stabilize the performance of the catalyst was performed before testing. Linear sweep voltammetry (LSV) was carried out at a scan rate of 1 mV s^{-1}, and electrochemical impedance spectroscopy (EIS) measurements were performed near the onset potential in the frequency range from 200 kHz to 10 mHz. The potential of E_{RHE} was calibrated by the equation of $E_{RHE} = E_{SCE} + 0.241\ V + 0.059 \cdot pH\ V$, consistent with the calibration results of the standard hydrogen electrode (RHE) (Figure S1). All LSV polarization curves were corrected against *iR* compensation. The electrochemical double layer capacitance (C_{dl}) measured by CV at different scan speeds was used to estimate the electrochemically active surface area (ECSA). The overall water splitting test was performed in a two-electrode system in the potential range of 0–2.0 V with a scan rate of 5 mV s^{-1} in 30% KOH solution.

Acknowledgements

This work has been supported by the National Natural Science Foundation of China (no. 21965005, 21963003), Natural Science Foundation of Guangxi Province (2018GXNSFAA294077, 2018GXNSFAA281220), Project of High-Level Talents of Guangxi (F-KA18015, 2018ZD004) and Guangxi Technology Base and Talent Subject (GUIKE AD18126001).

Conflict of Interest

The authors declare no conflict of interest.

Keywords: charge redistribution · electrocatalysis · nanoarrays · overall water splitting · P doping

[1] a) Y. Li, Z. Wang, J. Hu, S. Li, Y. Du, X. Han, P. Xu, *Adv. Funct. Mater.* **2020**, *30*, 1910498; b) M. Yang, Y. Jiang, M. Qu, Y. Qin, Y. Wang, W. Shen, R. He, W. Su, M. Li, *Appl. Catal. B* **2020**, *269*, 118803.
[2] a) G. Qian, G. Yu, J. Lu, L. Luo, T. Wang, C. Zhang, R. Ku, S. Yin, W. Chen, S. Mu, *J. Mater. Chem. A* **2020**, *8*, 14545–14554; b) Y. Li, X. Tan, H. Tan, H. Ren, S. Chen, W. Yang, S. C. Smith, C. Zhao, *Energy Environ. Sci.* **2020**, *13*, 1799–1807.
[3] a) W. Zhu, W. Chen, H. Yu, Y. Zeng, F. Ming, H. Liang, Z. Wang, *Appl. Catal. B* **2020**, *278*, 119326; b) H. Sun, C. Tian, G. Fan, J. Qi, Z. Liu, Z. Yan, F. Cheng, J. Chen, C.-P. Li, M. Du, *Adv. Funct. Mater.* **2020**, *30*, 1910596; c) S. Kurungot, R. Illathvalappil, F. Kanheerampockil, P. S. Walko, S. K. Bhat, R. N. Devi, *Chem. Eur. J.* **2020**, *26*, 7900–7911.
[4] a) F. Yu, H. Zhou, Y. Huang, J. Sun, F. Qin, J. Bao, W. A. Goddard, S. Chen, Z. Ren, *Nat. Commun.* **2018**, *9*, 2551; b) H. Zhou, F. Yu, Q. Zhu, J. Sun, F. Qin, L. Yu, J. Bao, Y. Yu, S. Chen, Z. Ren, *Energy Environ. Sci.* **2018**, *11*, 2858–2864.
[5] a) Q. Dang, Y. Sun, X. Wang, W. Zhu, Y. Chen, F. Liao, H. Huang, M. Shao, *Appl. Catal. B* **2019**, *257*, 117905; b) Y. Lee, J. Suntivich, K. J. May, E. E. Perry, Y. Shao-Horn, *J. Phys. Chem. Lett.* **2012**, *3*, 399–404.
[6] a) S. Y. Tee, K. Y. Win, W. S. Teo, L.-D. Koh, S. Liu, C. P. Teng, M.-Y. Han, *Adv. Sci.* **2017**, *4*, 1600337; b) Z. Wan, H. Yu, Q. He, Y. Hu, P. Yan, X. Shao, T. T. Isimjan, B. Zhang, X. Yang, *Int. J. Hydrogen Energy* **2020**, *45*, 22427–22436.
[7] a) K. N. Dinh, Y. Sun, Z. Pei, Z. Yuan, A. Suwardi, Q. Huang, X. Liao, Z. Wang, Y. Chen, Q. Yan, *Small* **2020**, *16*, 1905885; b) B. Wang, H. Huang, T. Sun, P. Yan, T. T. Isimjan, J. Tian, X. Yang, *J. Colloid Interface Sci.* **2020**, *567*, 339–346.
[8] H. Zhang, A. W. Maijenburg, X. Li, S. L. Schweizer, R. B. Wehrspohn, *Adv. Funct. Mater.* **2020**, *30*, 2003261.
[9] a) Y. Yu, J. Zhou, Z. Sun, *Adv. Funct. Mater.* **2020**, 2000570; b) L. He, W. Zhang, Q. Mo, W. Huang, L. Yang, Q. Gao, *Angew. Chem. Int. Ed.* **2020**, *59*, 3544–3548; *Angew. Chem.* **2020**, *132*, 3572–3576.
[10] a) X. F. Lu, Y. Chen, S. Wang, S. Gao, X. W. Lou, *Adv. Mater.* **2019**, *31*, 1902339; b) X. Tao, H. Xu, S. Luo, Y. Wu, C. Tian, X. Lu, Y. Qing, *Appl. Catal. B* **2020**, *279*, 119367.
[11] a) X. Huang, Z. Zeng, H. Zhang, *Chem. Soc. Rev.* **2013**, *42*, 1934–1946; b) T. F. Jaramillo, K. P. Jørgensen, J. Bonde, J. H. Nielsen, S. Horch, I. Chorkendorff, *Science* **2007**, *317*, 100–102.
[12] M. T. M. Koper, *Nat. Chem.* **2013**, *5*, 255–256.
[13] J. Hu, C. Zhang, L. Jiang, H. Lin, Y. An, D. Zhou, M. K. H. Leung, S. Yang, *Joule* **2017**, *1*, 383–393.
[14] B. Wang, H. Huang, M. Huang, P. Yan, T. T. Isimjan, X. Yang, *Sci. China Chem.* **2020**, *63*, 841–849.
[15] J. Hou, B. Zhang, Z. Li, S. Cao, Y. Sun, Y. Wu, Z. Gao, L. Sun, *ACS Catal.* **2018**, *8*, 4612–4621.
[16] a) K. Guruprasad, T. Maiyalagan, S. Shanmugam, *ACS Appl. Energy Mater.* **2019**, *2*, 6184–6194; b) A. Wu, C. Tian, H. Yan, Y. Jiao, Q. Yan, G. Yang, H. Fu, *Nanoscale* **2016**, *8*, 11052–11059.
[17] J. Lin, P. Wang, H. Wang, C. Li, X. Si, J. Qi, J. Cao, Z. Zhong, W. Fei, J. Feng, *Adv. Sci.* **2019**, *6*, 1900246.
[18] a) Y. Bai, H. Zhang, Y. Feng, L. Fang, Y. Wang, *J. Mater. Chem. A* **2016**, *4*, 9072–9079; b) K. He, T. Tadesse Tsega, X. Liu, J. Zai, X.-H. Li, X. Liu, W. Li, N. Ali, X. Qian, *Angew. Chem. Int. Ed.* **2019**, *58*, 11903–11909; *Angew. Chem.* **2019**, *131*, 12029–12035.
[19] a) X. Yang, A.-Y. Lu, Y. Zhu, M. N. Hedhili, S. Min, K.-W. Huang, Y. Han, L.-J. Li, *Nano Energy* **2015**, *15*, 634–641; b) G. Huang, W. Liang, Y. Wu, J. Li, Y. Q. Jin, H. Zeng, H. Zhang, F. Xie, J. Chen, N. Wang, Y. Jin, H. Meng, *J. Catal.* **2020**, *390*, 23–29; c) X. Huang, X. Xu, X. Luan, D. Cheng, *Nano Energy* **2020**, *68*, 104332.
[20] a) H. Yuan, S. Wei, B. Tang, Z. Ma, J. Li, M. Kundu, X. Wang, *ChemSusChem* **2020**, *13*, 3662–3670; b) D. Chen, H. Zhou, J. Xiao, A. Yuan, *ChemistrySelect* **2020**, *5*, 8233–8240; c) J. Feng, H. Zhou, J. Wang, T. Bian, J. Shao, A. Yuan, *Int. J. Hydrogen Energy* **2018**, *43*, 20538–20545.
[21] M. D. Sharma, C. Mahala, M. Basu, *Inorg. Chem.* **2020**, *59*, 4377–4388.
[22] T. Tang, Q. Gan, X. Guo, H. Dong, J. Zhang, Y. Zhao, J. Tian, X. Yang, *Sustain. Energ. Fuels* **2018**, *2*, 229–236.
[23] a) X. Guan, L. Zhao, P. Zhang, J. Liu, X. Song, L. Gao, *Mater. Today Energy* **2020**, *16*, 100379; b) L. Guo, X. Bai, H. Xue, J. Sun, T. Song, S. Zhang, L. Qin, K. Huang, F. He, Q. Wang, *Chem. Commun.* **2020**, *56*, 7702–7705.
[24] H. Zhao, Z. Li, X. Dai, M. Cui, F. Nie, X. Zhang, Z. Ren, Z. Yang, Y. Gan, X. Yin, Y. Wang, W. Song, *J. Mater. Chem. A* **2020**, *8*, 6732–6739.
[25] a) Y. Liu, Y. Xu, Y. Han, Z. Zhang, J. Xu, Y. Du, J. Bao, X. Zhou, *J. Power Sources* **2019**, *436*, 226860; b) P. Yan, M. Huang, B. Wang, Z. Wan, M. Qian, H. Yan, T. T. Isimjan, J. Tian, X. Yang, *J. Energy Chem.* **2020**, *47*, 299–306.
[26] a) A. Lim, J. Kim, H. J. Lee, H.-J. Kim, S. J. Yoo, J. H. Jang, H. Y. Park, Y.-E. Sung, H. S. Park, *Appl. Catal. B* **2020**, *272*, 118955; b) J.-L. Song, Z.-Q. Huang, B. Wang, D.-S. Pan, L.-L. Zhou, Z.-H. Guo, *ChemSusChem* **2020**, *13*, 2564–2570.
[27] a) H. Yu, Y. Xue, L. Hui, C. Zhang, Y. Zhao, Z. Li, Y. Li, *Adv. Funct. Mater.* **2018**, *28*, 1707564; b) K. Qi, X. Cui, L. Gu, S. Yu, X. Fan, M. Luo, S. Xu, N. Li, L. Zheng, Q. Zhang, J. Ma, Y. Gong, F. Lv, K. Wang, H. Huang, W. Zhang, S. Guo, W. Zheng, P. Liu, *Nat. Commun.* **2019**, *10*, 5231.
[28] J. Wang, H. Cheng, S. Ren, L. Zhang, L.-X. Ding, H. Wang, *J. Mater. Chem. A* **2020**, *8*, 16018–16023.
[29] A. Wu, Y. Gu, Y. Xie, C. Tian, H. Yan, D. Wang, X. Zhang, Z. Cai, H. Fu, *ACS Appl. Mater. Interfaces* **2019**, *11*, 25986–25995.
[30] Y. Du, H. Qu, Y. Liu, Y. Han, L. Wang, B. Dong, *Appl. Surf. Sci.* **2019**, *465*, 816–823.
[31] J. Zhang, T. Wang, D. Pohl, B. Rellinghaus, R. Dong, S. Liu, X. Zhuang, X. Feng, *Angew. Chem. Int. Ed.* **2016**, *55*, 6702–6707; *Angew. Chem.* **2016**, *128*, 6814–6819.
[32] X. Xia, Z. Zheng, Y. Zhang, X. Zhao, C. Wang, *Int. J. Hydrogen Energy* **2014**, *39*, 9638–9650.
[33] Y. Zhao, J. Zhang, X. Guo, H. Fan, W. Wu, H. Liu, G. Wang, *J. Mater. Chem. A* **2017**, *5*, 19672–19679.
[34] P. Liu, J. Zhu, J. Zhang, P. Xi, K. Tao, D. Gao, D. Xue, *ACS Energy Lett.* **2017**, *2*, 745–752.
[35] S. L. Zhang, B. Y. Guan, X. F. Lu, S. Xi, Y. Du, X. W. Lou, *Adv. Mater.* **2020**, *32*, 2002235.
[36] X. Huang, H. Xu, D. Cao, D. Cheng, *Nano Energy* **2020**, *78*, 105253.
[37] J. Liu, C. Wang, H. Sun, H. Wang, F. Rong, L. He, Y. Lou, S. Zhang, Z. Zhang, M. Du, *Appl. Catal. B* **2020**, *279*, 119407.
[38] a) K. Zhou, Y.-J. Tang, Y. Wang, *J. Mater. Chem. A* **2020**, *8*, 7925–7934; b) W. Zong, D. Rao, H. Guo, Y. Ouyang, Y.-E. Miao, W. Wang, J. Wang, F. Lai, T. Liu, *Nanoscale* **2020**, *12*, 10977–10986; c) H. Yuan, S. Wei, B. Tang, Z. Ma, J. Li, M. Kundu, X. Wang, *ChemSusChem* **2020**, *13*, 3662–3670; d) X. Zheng, P. Cui, Y. Qian, G. Zhao, X. Zheng, X. Xu, Z. Cheng, Y. Liu, S. X. Dou, W. Sun, *Angew. Chem. Int. Ed.* **2020**, *59*, 14533–14540; *Angew. Chem.* **2020**, *132*, 14641–14648; e) X. Zheng, X. Han, Y. Cao, Y. Zhang, D. Nordlund, J. Wang, S. Chou, H. Liu, L. Li, C. Zhong, Y. Deng, W. Hu, *Adv. Mater.* **2020**, *32*, 2000607; f) P. Thangasamy, S. Oh, S. Nam, H. Randriamahazaka, I.-K. Oh, *Small* **2020**, *16*, 2001665; g) C. He, M. Huang, G. Wang, Y. Zhang, X. Li, L. Fan, Y. Li, *Nanoscale* **2020**, *12*, 11735–11745; h) Q. Xia, H. Liu, M. Jin, L. Lai, Y. Qiu, H. Zhai, H. Li, X. Liu, *Nanoscale* **2020**, *12*, 8969–8974; i) Y. R. Hong, K. M. Kim, J. H. Ryu, S. Mhin, J. Kim, G. Ali, K. Y. Chung, S. Kang, H. Han, *Adv. Funct. Mater.* **2020**, *30*, 2004330; j) X. Wang, F. Li, W. Li, W. Gao, Y. Tang, R. Li, *J. Mater. Chem. A* **2017**, *5*, 17982–17989; k) T. Ouyang, X.-T. Wang, X.-Q. Mai, A.-N. Chen, Z.-Y. Tang, Z.-Q. Liu, *Angew. Chem. Int. Ed.* **2020**, *59*, 11948–11957; *Angew. Chem.* **2020**, *132*, 12046–12055; l) H. Shang, W. Sun, R. Sui, J. Pei, L. Zheng, J. Dong, Z. Jiang, D. Zhou, Z. Zhuang, W. Chen, J. Zhang, D. Wang, Y. Li, *Nano Lett.* **2020**, *20*, 5443–5450.
[39] M. Kim, M. A. R. Anjum, M. Choi, H. Y. Jeong, S. H. Choi, N. Park, J. S. Lee, *Adv. Funct. Mater.* **2020**, *30*, 2002536.

[40] a) A. I. Inamdar, H. S. Chavan, B. Hou, C. H. Lee, S. U. Lee, S. Cha, H. Kim, H. Im, *Small* **2020**, *16*, 1905884; b) J. H. Lin, H. H. Wang, J. Cao, F. He, J. C. Feng, J. L. Qi, *J. Colloid Interface Sci.* **2020**, *571*, 260-266; c) F.-T. Tsai, Y.-T. Deng, C.-W. Pao, J.-L. Chen, J.-F. Lee, K.-T. Lai, W.-F. Liaw, *J. Mater. Chem. A* **2020**, *8*, 9939-9950; d) L. Chen, Y. Song, Y. Liu, L. Xu, J. Qin, Y. Lei, Y. Tang, *J. Energy Chem.* **2020**, *50*, 395-401; e) R. Li, J. Zang, W. Li, J. Li, Q. Zou, S. Zhou, J. Su, Y. Wang, *ChemSusChem* **2020**, *13*, 3718-3725; f) G. Zhan, J. Zhang, Y. Wang, C. Yu, J. Wu, J. Cui, X. Shu, Y. Qin, H. Zheng, J. Sun, J. Yan, Y. Zhang, C. S. Tiwary, Y. Wu, *J. Colloid Interface Sci.* **2020**, *566*, 411-418; g) Y. Wang, S. Chen, S. Zhao, Q. Chen, J. Zhang, *J. Mater. Chem. A* **2020**, *8*, 15845-15852; h) Y. Chen, J. Yu, J. Jia, F. Liu, Y. Zhang, G. Xiong, R. Zhang, R. Yang, D. Sun, H. Liu, W. Zhou, *Appl. Catal. B: Environ.* **2020**, *272*, 118956.

[41] Y. Men, P. Li, J. Zhou, S. Chen, W. Luo, *Cell Rep. Phys. Sci.* **2020**, *1*, 100136.

[42] L. Ye, S. Chen, W. Li, M. Pi, T. Wu, D. Zhang, *J. Phys. Chem. C* **2015**, *119*, 9560–9567.

[43] a) J. Wang, F. Ciucci, *Appl. Catal. B* **2019**, *254*, 292–299; b) A. Muthurasu, V. Maruthapandian, H. Y. Kim, *Appl. Catal. B* **2019**, *248*, 202–210.

Manuscript received: December 15, 2020
Revised manuscript received: January 21, 2021
Accepted manuscript online: January 23, 2021
Version of record online: February 9, 2021